Contactless Vital Sign Monitoring During First Aid Using Handheld MmWave Radar

PAPER ID: 6666

tbw

Additional Key Words and Phrases: Long range sensing; LoRa; Soil moisture sensing.

ACM Reference Format:
Paper ID: 6666. 2023. Contactless Vital Sign Monitoring During First Aid Using Handheld MmWave Radar. *Proc. ACM Interact. Mob. Wearable Ubiquitous Technol.* 1, 1 (November 2023), 14 pages. https://doi.org/10.1145/nnnnnnn.nnnnnnn

1 INTRODUCTION

Administering first aid is crucial to save the life of a patient facing sudden and critical threats such as fainting, respiratory failure, and cardiac arrest. Timely first aid interventions can greatly influence patient outcomes, particularly in scenarios where every second can make the difference between survival or irreversible damage. Then, successful medical attention can be imperative to prevent death and reduce long-term health complications. Before and during first aid, it is essential to monitor vital signs, including respiratory rate (RR) and heart rate (HR). These indicators provide crucial insights into the overall functioning of the body and the severity of the medical emergency, thus guiding treatment decisions.

Traditional vital sign monitoring during first aid relies mainly on manual observation and measurements by rescuers. For instance, rescuers might observe the rise and fall of the chest, airflow from the nose, and touch the patient to feel the pulse to count RR and HR. However, medical practices have shown that manual observation and measurements may not be accurate, especially when performed by novices or in complex medical situations. The reliance on visual observation alone to monitor these vital signs can lead to inconsistencies and potential diagnosis errors. Furthermore, in high-stress emergency situations, even skilled medical professionals might face challenges in accurately assessing and interpreting these vital signs due to time constraints and the urgency of the circumstances. As a result, contact-based devices have been used to monitor vital signs. However, correctly setting up these devices can take time, particularly considering the stress of emergency situations, especially for inexperienced individuals. Additionally, there are instances where patients may not be suitable to wear these devices, such as when the area that needs to be worn has suffered an injury. Therefore, a contactless vital signs monitoring technology that is accurate, extremely user-friendly and quickly deployable is highly beneficial in emergency medical situations.

In recent years, wireless sensing-based vital sign monitoring technology has been extensively researched. Various wireless signals have been proven effective for contactless monitoring of a person's respiratory rate and waveform including WiFi [10, 13, 16], RFID [**?**], LoRa [15, 17, 19], LTE [9], mmWave [] and Ultra-Wideband (UWB) [18, 21]. Among these signals, mmWave and UWB radars have been shown to further monitor heartbeat due to their high frequency and large bandwidth [14, 21]. However, most existing studies have indicated that radars need to

Author's address: Paper ID: 6666.

2474-9567/2023/11-ART $15.00
https://doi.org/10.1145/nnnnnnn.nnnnnnn

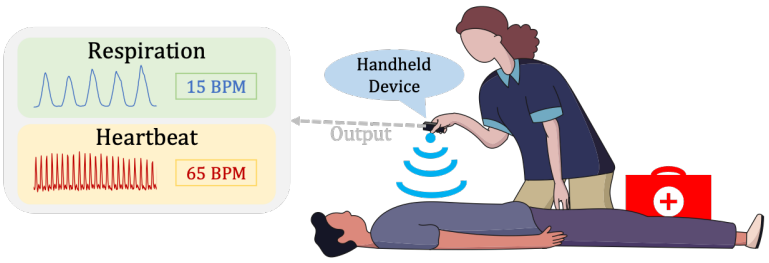

Fig. 1. Illustration of contactless vital sign monitoring using a handheld device.

be in a stationary state when sensing respiration and heartbeat, for example, placed on a table or mounted on a wall. Additionally, the radar needs to face the individual's body. However, in emergency scenarios, individuals may be lying in various environments, making it challenging to ensure that the radar can be placed in one location and keeps static to monitor vital signs. As illustrated in Figure 1, a more feasible approach would involve a handheld radar directed at the patient. However, when the radar is handheld, it inevitably experiences motion due to the involuntary shaking of the hand. Such device movement significantly interferes with the effectiveness of vital sign monitoring. This interference occurs because wireless sensing relies on estimating changes in the reflection path length of the human body to achieve vital sign monitoring. For instance, when a person breathes, chest movement causes variations in the distance between the radar and the chest, enabling the measurement of chest displacement. However, when the device itself is in motion, changes in the reflection path length of the human body include variations caused by the device's movement. Traditional signal processing methods find it challenging to separate the intended movement from device motion. This is because device motion typically exhibits random patterns and has displacements greater than the vital signs, overshadowing the target signal fluctuations.

To deal with the issue of device motion induced by hand movement, a recent work, Mobi^{2}Sense [20], proposes to eliminate the device motion by adopting a static object such as a chair in the environment as a reference. The key idea is the target-reflected signal and static object-reflected signal exhibit similar device motion patterns. Since the static object-reflected signal is only affected by device motion, and the target-reflected signal is affected by device motion and target motion (e.g., respiration), the static object-reflected signal can be used to cancel out the device motion component in the target-reflected signal. However, this work also reveals that the device motion-induced signal variations in the target-reflected signal and static object-reflected signal are not exactly the same. This is because the static object and target are at different directions with respect to the device motion direction. To this end, this work proposes a search-based scheme to estimate the difference between them and perform compensation before motion cancellation. However, through an experiment, we find that it cannot achieve HR monitoring. This shows that past work has not achieved the best device motion elimination performance as in static scenarios.

In this paper, we aim to push the limit of vital sign monitoring under device motion to achieve fine-grained heartbeat rate monitoring. First of all, we first conduct a thorough analysis to reveal why the previous work cannot achieve this. We notice that the proposed solution cannot completely eliminate the device motion. This is because the direction of device motion changes randomly in both time and spatial domains. Thus, without the estimation of device motion direction estimation, the previous work cannot obtain a precise compensation coefficient at fundamental level. Thus, the key of fine-grained device motion elimination lies in the accurate device motion direction estimation. In this paper, we propose to estimate the direction of device motion in advance

for device motion elimination. The key idea is utilizing two static objects in the environment for device motion direction estimation.

2 PRELIMINARY

In this section, we first introduce the background of mmWave radar based sensing and then present the sensing model under device motion.

2.1 mmWave radar based sensing

MmWave radar transmits signals in the millimeter wave frequency band. Most commercial mmWave radars modulate the signal utilizing frequency-modulated continuous wave (FMCW). The transmitted FMCW signal is composed of a series of chirps. A chirp is defined by its starting frequency f_c, bandwidth B and duration T. As shown in Figure 2a, the transmitted signal can be reflected by objects in the environment and propagates back to the radar. In the time domain, the object-reflected signal has a time delay compared to the transmitted signal, which also induces constant frequency differences in the frequency domain. FMCW radar mixes the transmitted signal and the received signal to generate the intermediate frequency (IF) signal, which consists of several frequency components:

$$s(t) = \sum_{n=1}^{N} A_n e^{j(2\pi \frac{2BR_n}{cT} t + \frac{4\pi f_c R_n}{c})}, \tag{1}$$

where N is the number of objects in the environment, A_n is the amplitude of the signal reflected by n-th object, R_n is the distance of the n-th object to radar and c is the speed of light. Equation 1 shows that the signals with different frequency components in the IF signal correspond to different reflecting objects, and the frequency ($\frac{2BR_n}{cT}$) is determined by the distance of the object. Therefore, performing Fourier transform on the IF signal can determine which frequency components are contained in the IF signal, thereby further inferring which distances there are objects reflecting signals. This operation is referred as Range-FFT. Then, the range profile can be obtained by performing Range-FFT on the IF signals at different times. Range profile shows at which distances objects exist. It is worth noting that due to the limited bandwidth, Range-FFT has a limited distance resolution, which is $R_{res} = \frac{c}{2B}$ [5]. The objects have a distance difference smaller than R_{res} fall into the same range bin on the range profile. As the example shown in Figure 2b, the reflected signal strength at 1 m, 2 m and 3 m is relatively strong, which corresponds to the reflected signals from the chair, the person, the TV, and the cabinet in the environment. Among them, the distance difference between the TV and cabinet is smaller than R_{res}. Thus, they mix together on the range profile.

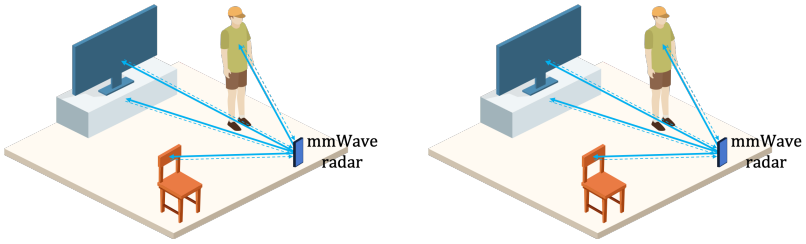

(a) Scenario of mmWave radar-based sensing.

(b) An example of the range profile.

Fig. 2. The basis of mmWave radar-based sensing.

After Range-FFT, the reflection signal from a static object (i.e., the i-th static object) is converted to:

$$y_{s,i}(t) = A_{s,i}e^{jKR_{s,i}}, \tag{2}$$

where $K = \frac{4\pi f_c}{c}$. Since the distance between this object to radar ($R_{s,i}$) does not change with time, $y_s(t)$ also remains constant with time. On the contrary, the reflected signal from target with micro-motion (e.g., breathing-induced chest movement) is represented as:

$$y_t(t) = A_t e^{jK(R_{tini}+R_{tmov}(t))}, \tag{3}$$

where R_{tini} is the initial range of the target and $\Delta R_{tmov}(t)$ is the displacement of movement. Thus, by extracting the phase change of the target-existed range bin ($\varphi_t(t)$), the target displacement can be obtained as:

$$R_{tmov}(t) = \frac{1}{K}\varphi_t(t) - R_{tini} = \frac{c}{4\pi f_c}\varphi_t(t) - R_{tini}. \tag{4}$$

This is the basic principle behind mmWave radar based sensing under static condition.

2.2 Sensing under device motion

In this section, we present the sensing model under device motion. When the device is moving, the change of distance between the target and the radar is also affected by device motion induced distance change ($R_{tdev}(t)$). Thus, the target-reflected signal should be modified as:

$$y_t(t) = A_t e^{jK(R_{tini}+R_{tmov}(t)+R_{tdev}(t))}. \tag{5}$$

It can be seen that now the phase change of target-reflected signal cannot be directly used to extract the target motion ($R_{tmov}(t)$) because device motion might be random and has a large scale. To address the effect of device motion on target motion extraction, a recent work, Mobi^{2}Sense [20], proposes to employ a static object in the environment as a reference to cancel out the device motion component in the phase of target-reflected signal. As shown in Figure 3a, the basic idea behind this solution is that device motion also generates phase change in the static object-reflected signal. Furthermore, the phase change patterns induced by device motion in target-reflected and static object-reflected signals are similar. Thus, the device motion induced phase change can first be estimated by extracting the static object-reflected signal. Then, it can be eliminated from the target-reflected signal. The signal reflected by the i-th static object in the presence of device motion can be written as:

$$y_{s,i}(t) = A_{s,i}e^{jK(R_{s,i}+R_{idev}(t))}, \tag{6}$$

where $R_{idev}(t)$ is the device motion induced distance variation of the i-th static object. Note that typically, device motion induced distance changes for the target ($R_{tdev}(t)$) and the static object ($R_{idev}(t)$) are different. As shown

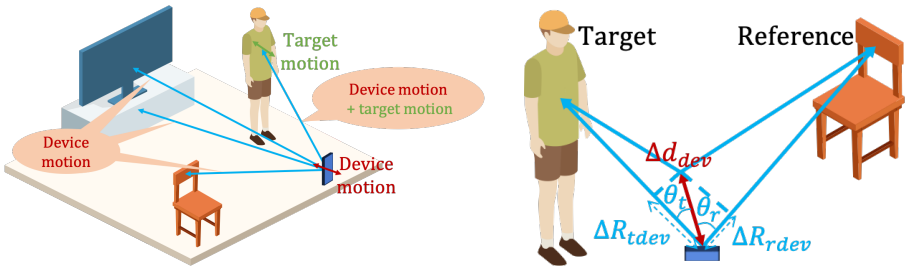

(a) Motion in each object-reflected path. (b) The effect of direction.

Fig. 3. The basis of sensing under device motion.

in Figure 3b, the directions of the target and the static object with respect to the device motion (θ_t and θ_i) can be different. Then, the device motion induced distance change between two adjacent signal samples at the two objects are $\Delta R_{tdev}(t) = R_{tdev}(t + \Delta t) - R_{tdev}(t) = \Delta d_{dev} \cos\theta_t$ and $\Delta R_{idev}(t) = R_{idev}(t + \Delta t) - R_{idev}(t) = \Delta d_{dev} \cos\theta_i$, respectively, where $\Delta d_{dev}(t)$ is the displacement of device motion and Δt is the time difference between two signal samples. Therefore, a coefficient $\beta_{t,i}(t)$ needs to be estimated in advance and then be compensated to the static object-reflected signal:

$$\beta_{t,i}(t) = \frac{\Delta R_{tdev}(t)}{\Delta R_{idev}(t)} = \frac{\Delta d_{dev}(t)\cos\theta_t(t)}{\Delta d_{dev}(t)\cos\theta_i(t)} = \frac{\cos\theta_t(t)}{\cos\theta_i(t)}. \tag{7}$$

The recent work [20] calculates the coefficient β using an optimization-based search scheme. However, we quickly find a fundamental drawback of search-based scheme. According to Equation 7, $\beta_{t,i}(t)$ is determined by the directions of the target and the static object with respect to the device motion direction (θ_t and θ_i). Thus, when the direction of device motion changes, $\beta_{t,i}(t)$ should also be modified. The direction change of device motion is typically random in time domain and spatial domain (e.g., involuntary shaking of the hand when holding the device). However, the solution in the previous work cannot estimate the direction of objects with respect to device motion direction. It simply sets a constant time interval and assumes that the device motion direction doesn't change in this time interval. Therefore, at the basic theoretical level, the previous work cannot completely eliminate the device motion.

We conduct an experiment to demonstrate the imperfect elimination of device motion. As shown in Figure 4a, a metal plate is used as the reference to cancel out the effect of device motion induced by hand movement on human respiration and heartbeat monitoring. Breathing and heartbeat movements simultaneously cause displacement of the chest. Since the displacement of breathing (4 - 12 mm [8]) is much larger than the displacement of heartbeat (0.2 - 0.5 mm [11]), extracting heartbeat from chest reflection signal is much more difficult than extracting breath. As shown in Figure 4b, when the device is static, the respiration waveform can be clearly observed from raw phase and heartbeat rate (HR) can be obtained from the FFT result on signal. However, when the device is held in hand, HR cannot be observed in the signal. In this paper, we propose a more fine-grained device motion elimination solution to break this limitation to achieve HR monitoring under device motion.

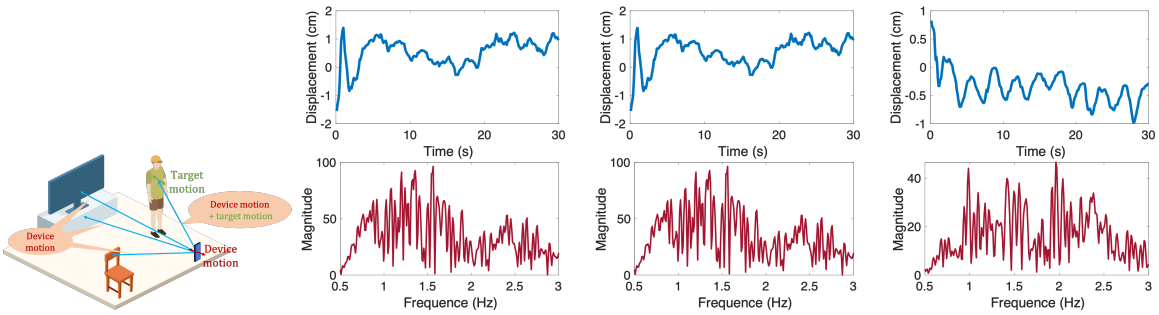

(a) Motion in each object-reflected path. (b) The effect of direction. (c) Motion in each object-reflected path. (d) The effect of direction.

Fig. 4. The basis of sensing under device motion.

3 FINE-GRAINED DEVICE MOTION ELIMINATION

In this section, we present a fine-grained device motion elimination approach to achieve heartbeat monitoring in the first aid scenario.

3.1 Device motion direction estimation

As introduced in Section 2.2, a key challenge of device motion elimination is the accurate calculation of the compensation coefficient β, which is determined by the direction of each object with respect to the device motion (θ_t and θ_i). Therefore, if these directions can be precisely estimated, the accurate β can be obtained. It is worth noting that the direction of an object with respect to the device motion is different from the direction with respect to the device. As shown in Figure 5a, θ_i and α is the direction of the i-th object with respect to the device and the direction of device motion with respect to the device, respectively. Then, the direction of the i-th object with respect to the device motion can be represented as:

$$\theta_{i,mov} = \theta_i + \alpha. \tag{8}$$

Therefore, the calculation of $\theta_{i,mov}$ can be decomposed to estimate the direction of the object and the device motion. Among them, the direction of the object relative to the device (θ_i) is relatively easy to estimate. Note that commercial mmWave radars are typically equipped with multiple antennas. Then, as shown in Figure 5b, the angle-of-arrival (AoA) of the received signal can be estimated leveraging the fact that the signal from θ leads to the same phase difference $\Delta\phi$ between each pair of adjacent antennas:

$$\Delta\phi = \frac{2\pi f_c d}{c} cos\theta, \tag{9}$$

where d is the distance between adjacent antennas. The AoA of the received signal can be estimated using Angle-FFT [7] across the received signals from all antennas. Then, the direction of each object with respect to the device (θ_i) can be obtained.

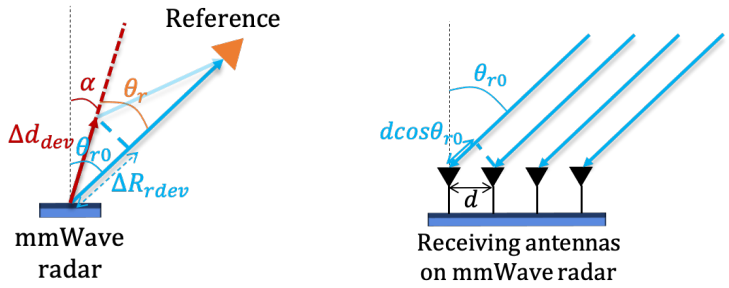

(a) The direction of the object with respect to the direction of device motion.

(b) The principle behind AoA estimation.

Fig. 5. Illustration of the direction of the object.

Then, the direction of device motion must be estimated. In this paper, we propose a novel solution for device motion direction estimation using two static objects as references. The main idea is that the phase changes of

two static objects' reflection signals are only induced by device motion. According to Equation 7, the relationship between the change in path length of two static objects is:

$$\frac{\Delta R_{s1}(t)}{\Delta R_{s2}(t)} = \frac{\cos(\theta_1 + \alpha)}{\cos(\theta_2 + \alpha)}. \tag{10}$$

Then, the device motion direction α can be calculated by solving an optimized function:

$$\arg\min_{\alpha} \left| \frac{\Delta R_{s1}(t)}{\Delta R_{s2}(t)} - \frac{\cos(\theta_1 + \alpha)}{\cos(\theta_2 + \alpha)} \right|, \tag{11}$$

where θ_1 and θ_2 can be estimated using Angle-FFT, and the distance changes $\Delta R_{s1}(t)$ and $\Delta R_{s2}(t)$ can be obtained by calculating the phase difference two adjacent signal samples and then employing Equation 3.

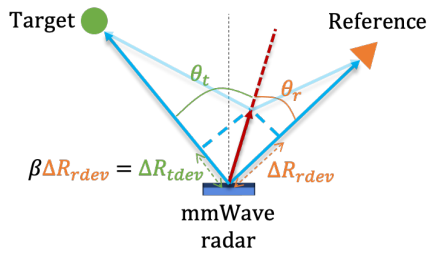

Fig. 6. Illustration of device motion elimination.

3.2 Device motion cancellation

First, the direction of the target with respect to the device (θ_t) is estimated using Angle-FFT. Then, since the direction of device motion $\alpha(t)$ is obtained, the compensation coefficient β can be calculated directly based on Equation 7 to eliminate the motion of the device. We extract the phase of the i-th static object's reflection signal based on Equation 6:

$$\varphi_i(t) = K(R_{iini} + R_{idev}(t)). \tag{12}$$

Then, the distance change at each moment can be calculated as:

$$\Delta R_{idev}(t) = R_{idev}(t + \Delta t) - R_{idev}(t) = \frac{\varphi_i(t + \Delta t) - \varphi_i(t)}{K}. \tag{13}$$

Meanwhile, the distance change at each moment of the target can be obtained in the same way using the phase of target-reflected signal:

$$\Delta R_t(t) = \Delta R_{tmov}(t) + \Delta R_{tdev}(t). \tag{14}$$

To eliminate the term of device motion $\Delta R_{tdev}(t)$, we first calculate the compensation coefficient between the target and the i-th static object: $\beta_{t,i} = \frac{cos(\theta_t(t)+\alpha(t))}{cos(\theta_i(t)+\alpha(t))}$. Note that according to Equation 10, $\beta_{t,i} = \frac{\Delta R_{tdev}(t)}{\Delta R_{idev}(t)}$. Thus, we can eliminate the device motion induced distance change of target leveraging the distance change of the static object and the compensation coefficient:

$$\begin{aligned} \Delta R_{tnew}(t) &= \Delta R_t(t) - \beta_{t,i}(t)\Delta R_{idev}(t) \\ &= \Delta R_{tmov}(t) + \Delta R_{tdev}(t) - \Delta R_{tdev}(t) \\ &= \Delta R_{tmov}(t). \end{aligned} \tag{15}$$

Finally, the target movement can be restored from distance change as:

$$R_{tmov}(t) = \sum_{m=0}^{t} \Delta R_{tnew}(m) = \sum_{m=0}^{t} \Delta R_{tmov}(m), \tag{16}$$

where m is the index of signal sample in the time domain.

4 SYSTEM IMPLEMENTATION AND DESIGN

4.1 Hardware implementation

We prototype the proposed solution based on a commercial mmWave radar, which is TI IWR1843BOOST [3]. The radar is set to transmit FMCW signals at a starting frequency of 77 GHz with a bandwidth of 4 GHz. The radar is set to Multiple-Input Multiple-Output (MIMO) mode, in which two transmitting antennas send signals in time division, and four receiving antennas receive signals simultaneously. The raw received IF signals are collected by the TI DCA1000EVM [2] data acquisition board and sent to a laptop through an Ethernet connection. The connected laptop is also used to set the radar parameters and control signal transmitting with MMWAVE-STUDIO [4]. A Macbook Pro with an Intel Core i7 processor and 32GB memory is used for data processing in MATLAB.

4.2 System design

Figure 7 illustrates the overview of our system, which contains three key modules: signal preprocessing, device motion direction estimation, and device motion elimination.

- **Signal preprocessing:** This module takes the raw signals captured by the mmWave radar as input. By performing Range-FFT and AoA estimation algorithms, the Range-Angle profile can be generated.
- **Device motion direction estimation:** By analyzing the Range-Angle profile, the direction of each static object and human target can be obtained, and the corresponding reflected signals can be extracted employing beamforming. Then, the direction of device motion can be estimated. We also introduce the requirement of static objects in real-world environment.
- **Device motion elimination:** Given the estimated device motion direction, the device motion component in human-reflected signal can be eliminated. Then, RR and HR can be calculated as the output.

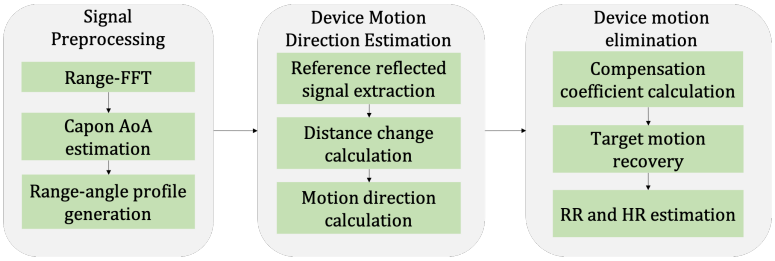

Fig. 7. Overview of system design.

4.3 Signal preprocessing

In this module, we process the raw signal samples captured by the radar hardware. The raw data collected by the radar is the IF signal of each chirp. For each chirp and each receiving antenna, we convert the raw IF signal into

the range profile using Range-FFT. Then, by performing 2D Capon beamforming [6] on each range bin across all receiving antennas, the range-angle profile can be obtained.

4.4 Device motion direction estimation

As introduced in Section 3.1, estimating the direction of device motion relies on the reflected signals from static objects in the environment. In the first aid scenario, sensing target (patient) typically lies on the ground and the radar is in front of her/his chest as shown in Figure 1. In this case, The ground is expected to be the static object that can be used to efficiently estimate the direction of device motion. Initially, we expect the ground on both sides of the human target can be used as static objects. However, we quickly find a serious issue, that is, because the surface is relatively large and smooth, the ground usually reflects RF signals in the form of mirror reflection. Figure 8a illustrates the effect of mirror reflection. The angle of reflection of the RF signal is equal to the angle of incidence. Because the incidence angle is large, the majority of the incident signal is reflected into the environment rather than back to the radar and received. The effect of mirror reflection could seriously reduce the signal-to-noise ratio (SNR) of ground-reflected signals. Thus, we think that the ground is not a good static object for estimating the direction of device motion.

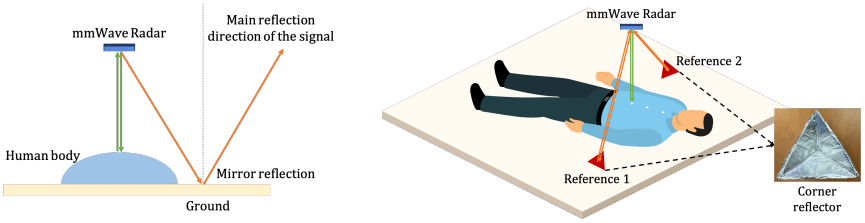

(a) The direction of the object with respect to the direction of device motion.

(b) The principle behind AoA estimation.

Fig. 8. Illustration of the direction of the object.

To deal with this issue, we propose to place two low-cost corner reflectors around the person as static objects to estimate the direction of device motion. A corner reflector is a retroreflector consisting of three mutually perpendicular, intersecting flat surfaces, which reflects RF signals directly towards the source. In this work, we handmade three corner reflectors using cardboard and tinfoil. As shown in Figure 8b, corner reflectors are placed around the patient on the ground. Figure 9a shows an example of the range-angle profile under this setting. Four obvious areas of strong reflected signal strength can be observed on the range-angle profile. Among them, the largest area corresponds to the human target, because when the radar is in front of the body, there are reflected signals from body within plus and minus 20 degrees. The other three smaller areas correspond to three corner reflectors, because the corner reflections can be regarded as single-point reflections. We employ the Constant False Alarm Rate (CFAR) [12] detection approach on the range-angle profile. The CFAR algorithm serves to identify the presence of objects within a background of noise by adaptively comparing the magnitude of adjacent bins. Consequently, we can identify the bins corresponding to human body and corner reflectors reflected signals, thereby acquiring the distance and direction of these objects. Then, we beamform the receiving signals to the direction of each object to obtain the corresponding reflected signal. Based on the reflected signals from corner reflectors, we first extract the phase and calculate the phase change at each moment. Then, we can calculate the direction of device motion using Equation 11.

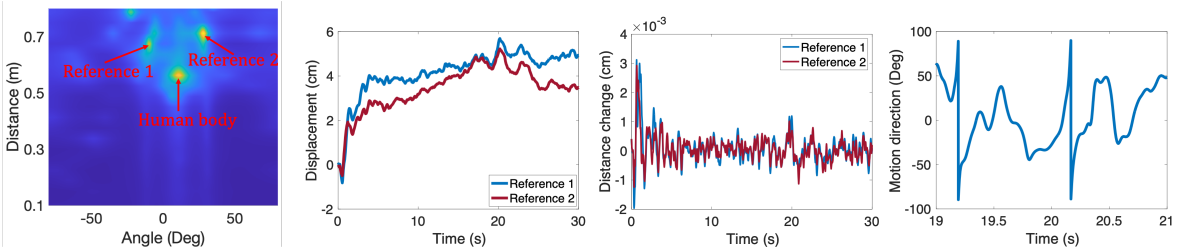

(a) Motion in each object-reflected path. (b) The effect of direction. (c) Motion in each object-reflected path. (d) The effect of direction.

Fig. 9. The basis of sensing under device motion.

4.5 Device motion elimination

After obtaining the direction of device motion, we can further eliminate the device motion component in the human-reflected signal. Note that theoretically, all three corner reflectors can be used as the reference. We propose to select the one with the strongest reflected signal strength as the reference. The reason behind this choice is the stronger signal strength indicates the better SNR. Based on the direction of human target, the direction of the reference and direction of device motion, we first calculate the compensation coefficient β. Then, β is multiplied to the path length change of the reference-reflected signal to obtain the device motion-induced path length change at the direction of human target. Thus, the device motion component can be subtracted from the path length change of human-reflected signal. Finally, target motion displacement can be recovered based on Equation 16. In this progress, we observe an issue that affects the performance of device motion elimination. We find that when the reference is close to 90° relative to the device movement direction, a very large change occurs in the target-reflected path displacement after eliminating the device movement. As shown in Figure 10a, when the direction is 90.3°, we can observe a distance change of 1 m, which is unreasonable for vital sign-induced motion. This issue can be interpreted by analyzing the equation of the compensation coefficient $\beta_{r,t}(t) = \frac{cos(\theta_t(t)+\alpha(t))}{cos(\theta_r(t)+\alpha(t))}$. When the direction of the reference $(\theta_r(t) + \alpha(t))$ is close to $90degree$, the value of the denominator is close to zero, inducing a large distance change. As shown in Figure 10b, in this condition, the direction of device motion is perpendicular to the direction of the reference object. Device motion-induced path length change for reference approaches zero and $cos(\theta_r(t) + \alpha(t))$ approaches infinity. Thus, an unpredictable error occurs at this time.

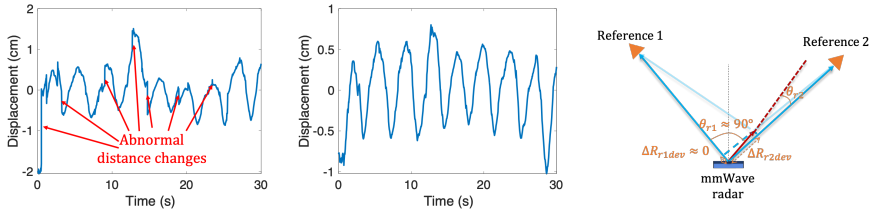

(a) Motion in each object-reflected path. (b) The effect of direction. (c) Motion in each object-reflected path.

Fig. 10. The basis of sensing under device motion.

To address this issue, we utilize a key observation, which is when the direction of the reference is perpendicular to the device motion, the directions of other static objects are not 90°. Intuitively, we can change another reference in this condition. To this end, we continuously monitor the direction of the reference with respect to the direction of device motion. When the angle is greater than 85°, we temporarily switch another object as the reference for calculating the length change of the target-reflected path caused by device movement. As shown in Figure 10c, based on the proposed scheme, the newly calculated device motion at the direction of human target is smooth, and therefore there are no distance sudden changes in the restored target motion displacement.

5 EVALUATION

In this section, we evaluate the performance of the proposed system. First, we conduct two benchmark experiments in a laboratory environment to validate the effectiveness of the proposed approaches, including the estimation of device motion direction and device motion elimination. We study the impact of varying parameters and settings. Then, we verify the performance of respiration and heartbeat monitoring in real-world environments.

5.1 Evaluation on Device Motion Direction Estimation

5.1.1 Experiment Setup: Figure **??** shows the experiment environment and setup. The mmWave radar is placed on a sliding track which can be controlled by Raspberry Pi. Then, we simulate the device motion by controlling the motion of the sliding track. Two corner reflectors are placed in front of the radar, which are used for device motion direction estimation. By default, the distance from the reflectors to the radar is 1 m, and the angles are 30° and -30°, respectively.

5.1.2 Overall Performance: As shown in Figure **??**, we present the overall performance of all the experiment settings. The proposed approach achieves a median device motion direction estimation error of 3.57°. Figure **??** shows an example of direction estimation result when the radar moves 1 cm in the direction of 0°. As shown in the figure, the maximum direction estimation error during movement does not exceed 5° and the average error is less than 3°.

5.1.3 Impact of Device Motion Direction: In this experiment, we vary the direction of device motion from 0° to 360° at a step of 30°. Figure **??** shows that for each device motion direction, the median estimation error is less than 4°. There is no significant difference in the errors estimated by the system for different motion directions. This shows that our method can effectively estimate different device motion directions with high accuracy.

5.1.4 Impact of Device Motion Scale: In this experiment, we change the scale of device motion from 1 cm to 5 cm at a step of 1 cm. The direction of device motion keeps 0°. As shown in Figure **??**, our system works with an error less than 4° for different motion scales. Note that the scale of hand motion induced by involuntary hand shaking is typically less than 1 cm. Thus, this experiment implies our approach is sufficient to estimate the direction of involuntary hand movements.

5.1.5 Impact of Corner Reflector Position: In this experiment, we evaluate the performance of motion direction estimation under different corner reflector positions (i.e., distance and angle). We first change the distance between the radar and reflectors from 0.5 m to 2 m at a step of 0.5 m. Then, at a distance of 1 m, we vary the angle of one reflector from 0° to 60° at a step of 20° while keeping the angle of another reflector at -30°. As shown in Figure **??**, for each setting, the direction estimation error is less than 3.4°, which indicates our system can accurately estimate device motion direction under various possible position relationships in real-world deployments.

5.2 Evaluation on device motion elimination

5.2.1 Experiment Setup: As shown in Figure **??**, we use a metal plate with a size of $10 \times 15\ cm^2$ as the sensing target. The metal plate is placed on a sliding track. Then, we simulate the displacement of the chest caused by human respiration and heartbeat by controlling the periodic reciprocating motion of the metal plate. The period of target motion is set to 1 Hz. Two corner reflectors are placed on the sides of the metal plate, which are used for device motion direction estimation and device motion elimination. A participant holds the radar facing the sensing target (the metal plate). A LiDAR is used to capture the ground truth of target motion.

5.2.2 Impact of Target Motion Scale: In this experiment, we evaluate different scales of target motion, including 0.5 mm, 1 mm, 2 mm, 5 mm, 10 mm. Figure **??** shows the similarity between the extracted phase with and without device motion elimination, and the ground truth measurement. It can be seen that for all target motion scales, the similarity is greater than 90% with device motion elimination. We further calculate the accuracy of displacement estimation. Figure **??** shows that the relative errors are below 5%. Note that the displacement of respiration and heartbeat-induced chest motion is 4 - 12 mm [8] and 0.2 - 0.5 mm [11], respectively. Thus, respiration and heartbeat monitoring are feasible using our method.

5.2.3 Impact of Person Holding Device: In reality, different people may have different patterns of involuntary hand shaking. Therefore, we recruit five participants to hold the radar. The target motion displacement scale is set to 0.5 mm. As shown in Figure **??**, the similarity for each participant is greater than 85% and the displacement estimation error is less than 10%.

5.2.4 Impact of Corner Reflector Position: To evaluate the effect of reflector position on device motion elimination, we repeat the experiment setup conducted in Section 5.1.5. As shown in Figure **??**, the similarity for each setting is greater than 85% and the displacement estimation error is less than 10%.

5.3 Evaluation in Real-world Environments

In this section, we evaluate the performance of respiration and heartbeat monitoring.

5.3.1 Experiment Setup: As shown in Figure **??**, a person lies on the ground as the target, with two corner reflectors placed on both sides of the body. Another person holds the radar next to the target and points it at the target's chest. The ground truth of respiration and heartbeat is measured by wearable sensors. Respiration waveform is measured using a NUL-236 belt [1] worn on the target's belly. The heartbeat ECG is collected by a xxx light sensor [] clipped to a finger. Then we calculate the ground truth RR and HR using the collected ground truth waveform. We compare our system with the baseline method Mobi^{2}Sense [20].

5.3.2 Overall Performance: overall performance
different person
different distance
different environment
with and without corner reflectors

6 RELATED WORK

Wireless sensing: In recent years, researchers have explored the use of various wireless signals for sensing including WiFi [13**? ?**], RFID [**? ?**], LoRa [15, 17, 19], LTE [9**? ?**], UWB [14**? ?**], mmWave [**? ? ?**] and acoustic signals [**? ? ?**]. Among them, mmWave radar, UWB and acoustic signal can support passive localization of targets due to their large bandwidth and high distance resolution. Meanwhile, many common commercial mmWave radars have been configured with multiple antennas to support angle estimation and beamforming. Therefore, in this paper, we choose to implement MSense using a commercial mmWave radar. Due to its high range and angle

resolution brought by large bandwidth and multiple antennas, mmWave radar has been widely used in a large number of sensing applications. However, most of these works assume that the human target and the radar need to be stationary during sensing process. In this paper, we bring the ability to resist body and device motion to mmWave radar sensing and support a variety of useful sensing applications.

Device motion elimination: A recent work [20] proposes to eliminate device motion using UWB radar. The principle behind it is the device motion can be estimated by extracting the signal reflected from a static object in the environment. Then, the device motion component can be canceled out from the target reflected signal. However, this approach cannot deal with body motion because the static object reflected signal does not contain body motion information. On the other hand, several approaches [**? ? ? ?**] have been explored to utilize deep learning methods to decompose and recover vital sign signals from complex signals affected by body motions. The underlying idea behind these methods is that the periodicity or correlation of fluctuations in the temporal domain of vital sign signals differs significantly from those caused by body movements. According to the basic principle, existing methods are limited to only separating and restoring periodic target motions. However, in many applications like activity detection and gesture recognition, sensing target signals can be aperiodic. Hence, previous research exhibits poor generalization capabilities when applied to aperiodic sensing tasks. In this paper, we take body and device motion elimination simultaneously into consideration for the first time. Furthermore, the proposed scheme is based on signal processing without a need of training or learning. Thus, our approach can be applied to sense both periodic and aperiodic target motions.

7 DISCUSSION

8 CONCLUSION

REFERENCES

[1] 2017. Respiration Monitor Belt logger sensor NUL-236. https://neulog.com/respiration-monitor-belt/.

[2] 2023. DCA1000EVM. https://www.ti.com/tool/DCA1000EVM.

[3] 2023. IWR1843BOOST. https://www.ti.com/product/IWR1843BOOST/part-details/IWR1843BOOST.

[4] 2023. MMWAVE-STUDIO. https://www.ti.com/tool/MMWAVE-STUDIO.

[5] Fadel Adib, Chen-Yu Hsu, Hongzi Mao, Dina Katabi, and Frédo Durand. 2015. Capturing the human figure through a wall. *ACM Transactions on Graphics (TOG)* 34, 6 (2015), 1–13.

[6] Jack Capon. 1969. High-resolution frequency-wavenumber spectrum analysis. *Proc. IEEE* 57, 8 (1969), 1408–1418.

[7] Weiyan Chen, Hongliu Yang, Xiaoyang Bi, Rong Zheng, Fusang Zhang, Peng Bao, Zhaoxin Chang, Xujun Ma, and Daqing Zhang. 2023. Environment-aware Multi-person Tracking in Indoor Environments with MmWave Radars. *Proceedings of the ACM on Interactive, Mobile, Wearable and Ubiquitous Technologies* 7, 3 (2023), 1–29.

[8] Anne De Groote, Muriel Wantier, Guy Chéron, Marc Estenne, and Manuel Paiva. 1997. Chest wall motion during tidal breathing. *Journal of Applied Physiology* 83, 5 (1997), 1531–1537.

[9] Yuda Feng, Yaxiong Xie, Deepak Ganesan, and Jie Xiong. 2021. Lte-based pervasive sensing across indoor and outdoor. In *Proceedings of the 19th ACM Conference on Embedded Networked Sensor Systems*. 138–151.

[10] Kai Niu, Fusang Zhang, Zhaoxin Chang, and Daqing Zhang. 2018. A fresnel diffraction model based human respiration detection system using COTS Wi-Fi devices. In *Proceedings of the 2018 ACM international joint conference and 2018 international symposium on pervasive and ubiquitous computing and wearable computers*. 416–419.

[11] G Ramachandran and M Singh. 1989. Three-dimensional reconstruction of cardiac displacement patterns on the chest wall during the P, QRS and T-segments of the ECG by laser speckle inteferometry. *Medical and Biological Engineering and Computing* 27 (1989), 525–530.

[12] Frank C Robey, Daniel R Fuhrmann, Edward J Kelly, and Ramon Nitzberg. 1992. A CFAR adaptive matched filter detector. *IEEE Transactions on aerospace and electronic systems* 28, 1 (1992), 208–216.

[13] Hao Wang, Daqing Zhang, Junyi Ma, Yasha Wang, Yuxiang Wang, Dan Wu, Tao Gu, and Bing Xie. 2016. Human respiration detection with commodity WiFi devices: Do user location and body orientation matter?. In *Proceedings of the 2016 ACM international joint conference on pervasive and ubiquitous computing*. 25–36.

[14] Zhi Wang, Beihong Jin, Siheng Li, Fusang Zhang, and Wenbo Zhang. 2023. ECG-grained Cardiac Monitoring Using UWB Signals. *Proceedings of the ACM on Interactive, Mobile, Wearable and Ubiquitous Technologies* 6, 4 (2023), 1–25.

[15] Binbin Xie, Minhao Cui, Deepak Ganesan, Xiangru Chen, and Jie Xiong. 2023. Boosting the Long Range Sensing Potential of LoRa. In *Proceedings of the 21st Annual International Conference on Mobile Systems, Applications and Services*. 177–190.

[16] Youwei Zeng, Dan Wu, Jie Xiong, Enze Yi, Ruiyang Gao, and Daqing Zhang. 2019. FarSense: Pushing the range limit of WiFi-based respiration sensing with CSI ratio of two antennas. *Proceedings of the ACM on Interactive, Mobile, Wearable and Ubiquitous Technologies* 3, 3 (2019), 1–26.

[17] Fusang Zhang, Zhaoxin Chang, Kai Niu, Jie Xiong, Beihong Jin, Qin Lv, and Daqing Zhang. 2020. Exploring lora for long-range through-wall sensing. *Proceedings of the ACM on Interactive, Mobile, Wearable and Ubiquitous Technologies* 4, 2 (2020), 1–27.

[18] Fusang Zhang, Zhaoxin Chang, Jie Xiong, Junqi Ma, Jiazhi Ni, Wenbo Zhang, Beihong Jin, and Daqing Zhang. 2023. Embracing Consumer-level UWB-equipped Devices for Fine-grained Wireless Sensing. *Proceedings of the ACM on Interactive, Mobile, Wearable and Ubiquitous Technologies* 6, 4 (2023), 1–27.

[19] Fusang Zhang, Zhaoxin Chang, Jie Xiong, Rong Zheng, Junqi Ma, Kai Niu, Beihong Jin, and Daqing Zhang. 2021. Unlocking the beamforming potential of LoRa for long-range multi-target respiration sensing. *Proceedings of the ACM on Interactive, Mobile, Wearable and Ubiquitous Technologies* 5, 2 (2021), 1–25.

[20] Fusang Zhang, Jie Xiong, Zhaoxin Chang, Junqi Ma, and Daqing Zhang. 2022. Mobi2Sense: empowering wireless sensing with mobility. In *Proceedings of the 28th Annual International Conference on Mobile Computing And Networking*. 268–281.

[21] Tianyue Zheng, Zhe Chen, Chao Cai, Jun Luo, and Xu Zhang. 2020. V2iFi: In-vehicle vital sign monitoring via compact RF sensing. *Proceedings of the ACM on Interactive, Mobile, Wearable and Ubiquitous Technologies* 4, 2 (2020), 1–27.